In the format provided by the authors and unedited.

Combined multi-plane phase retrieval and super-resolution optical fluctuation imaging for 4D cell microscopy

A. Descloux [1,6], K. S. Grußmayer [1,6], E. Bostan[2,4], T. Lukes[1], A. Bouwens [1], A. Sharipov[1], S. Geissbuehler[1], A.-L. Mahul-Mellier[3], H. A. Lashuel[3], M. Leutenegger[1,5] and T. Lasser [1*]

[1]École Polytechnique Fédérale de Lausanne, Laboratoire d'Optique Biomédicale, Lausanne, Switzerland. [2]École Polytechnique Fédérale de Lausanne, Biomedical Imaging Group, Lausanne, Switzerland. [3]École Polytechnique Fédérale de Lausanne, Laboratory of Molecular and Chemical Biology of Neurodegeneration, Brain Mind Institute, Lausanne, Switzerland. [4]Present address: University of California, Berkeley, Computational Imaging Lab, Berkeley, CA, USA. [5]Present address: Max-Planck Institute for Biophysical Chemistry, Department of NanoBiophotonics, Göttingen, Germany. [6]These authors contributed equally: A. Descloux and K. S. Grußmayer. *e-mail: theo.lasser@epfl.ch

Combined Multi-Plane Phase Retrieval and Super-Resolution Optical Fluctuation Imaging for 4D Cell Microscopy - Supplementary Material

Contents

Combined Multi-Plane Phase Retrieval and Super-Resolution Optical Fluctuation Imaging for 4D Cell Microscopy - Supplementary Material

1   Polychromatic light scattering

1.1   Monochromatic scattering[1]

Following the seminal work of Born & Wolf[1], we consider a monochromatic scalar electromagnetic field $U(x)$ at frequency ω (assuming a slowly varying refractive index $n(x)$). This electromagnetic field has to satisfy the Helmholtz equation

$$(\nabla^2 + k_0^2 n^2(x))U(x) = 0, \tag{S1}$$

where $x = (x, y, z)$ is the spatial coordinate, $\nabla^2 = \frac{\partial^2}{\partial x^2} + \frac{\partial^2}{\partial y^2} + \frac{\partial^2}{\partial z^2}$ is the Laplacian operator, $k_0 = \frac{\omega}{c} = \frac{2\pi}{\lambda}$ the wavenumber of the electromagnetic field in vacuum and $n(x)$ being the spatial refractive index distribution of the sample.

Equation (S1) cannot be solved in general due to the spatially varying refractive index. We therefore take the index of refraction to vary around the mean refractive index $\bar{n}$. Equation (S1) can now be rewritten as

$$(\nabla^2 + k_0^2 \bar{n}^2)U(x) = -F(x)U(x), \tag{S2}$$

where $F(x) = k_0^2(n^2(x) - \bar{n}^2)$ is the scattering potential.

The left-hand side of equation (S2) is the homogeneous wave equation, whereas the right hand side represents a source term containing the scattering potential $F(x)$.

Outside of the scattering volume, the total field is written as a superposition of the incident field and the scattered field

$$U(x) = U_i(x) + U_s(x). \tag{S3}$$

Using the homogeneous Helmholtz equation for the incident field $U_i(x)$, we obtain

$$(\nabla^2 + \bar{n}^2 k_0^2)U_i(x) = 0. \tag{S4}$$

By combining equations (S2) and (S3) and using (S4), we write for the scattered field $U_s(x)$, which satisfies the inhomogeneous Helmholtz equation

$$[\nabla^2 + k_0^2 \bar{n}^2]U_s(x) = -F(x)U(x). \tag{S5}$$

---

[1] Throughout all the calculations we use the same notation for the intensity and its Fourier transformed spectrum. The distinction is made by explicitly noting the variable x or g and the bold font is reserved for the spatial coordinates in three dimensions, i.e. $x = (x, y, z)$ and $g = (g_\perp, g_z)$, with $g_\perp$ shorthand for (g_x, g_y). The wavenumber, i.e. the magnitude of the wave vector, is denoted as $k_0 = \sqrt{k_\perp^2 + k_z^2} = \frac{2\pi}{\lambda} = \frac{\omega}{c}$.

Combined Multi-Plane Phase Retrieval and Super-Resolution Optical Fluctuation Imaging for 4D Cell Microscopy - Supplementary Material

Using a Green's function ansatz[1] we write

$$[\nabla^2 + k_0^2\,\bar{n}^2]G(\boldsymbol{x} - \boldsymbol{x}') = -\delta(\boldsymbol{x} - \boldsymbol{x}').$$ (S6)

where $\delta(\boldsymbol{x} - \boldsymbol{x}')$ is the 3D Dirac function.

Approximating the far-field response of a point scatterer as a spherical wave, we have

$$G(\boldsymbol{x} - \boldsymbol{x}') = \frac{e^{ik_0|\boldsymbol{x} - \boldsymbol{x}'|}}{|\boldsymbol{x} - \boldsymbol{x}'|}.$$ (S7)

Because the scattered field is much weaker than the incident field (first-order Born approximation), we neglect the scattered field in comparison to the dominant incident field. We obtain outside of the scattering volume V_s for the scattering field

$$U_s(\boldsymbol{x}) = \int_{V_s} G(\boldsymbol{x} - \boldsymbol{x}')F(\boldsymbol{x}')U_i(\boldsymbol{x}')\mathrm{d}^3x'.$$ (S8)

This represents a 3D convolution of the source term $F(\boldsymbol{x}')U_i(\boldsymbol{x}')$ with the Green's function. The Green's function (equation (S7)) can be expressed by a series expansion (Weyl's expansion of a spherical wave in terms of plane waves) in the lateral coordinate x and y as[2,3]

$$G(\boldsymbol{x} - \boldsymbol{x}') = \frac{i}{2\pi k_z} \iint_{-\infty}^{\infty} e^{i\left(k_x(x-x')+k_y(y-y')+k_z(z-z')\right)} \mathrm{d}k_x \mathrm{d}k_y.$$ (S9)

Inserting equation (S9) into (S8) and taking a Fourier transform, we use the convolution theorem and obtain for $U_s(\boldsymbol{k}; z)$ in Fourier space

$$U_s(\boldsymbol{k}; z) = \frac{i}{k_z} e^{ik_z z}[F(\boldsymbol{g}) \otimes_{\boldsymbol{k}} U_i(\boldsymbol{g})],$$ (S10)

where $\boldsymbol{g}$ is the object spatial frequency space and $\boldsymbol{k}$ is the scattered field spatial frequency space, $\otimes_{\boldsymbol{k}}$ is the convolution operator evaluated at $\boldsymbol{k}$, $e^{ik_z z}$ represents the propagation of the wave and $k_z = \bar{n}k_0 \cos(\theta_{det})$ represents the projection of the scattering vector $\boldsymbol{k}$ onto the optical axis (where we follow the derivation of Singer et al.[4]).

Assuming a monochromatic plane wave (in Fourier space) with an amplitude A, propagating along the direction $\boldsymbol{k}_i$ for the incident field $U_i(\boldsymbol{g}; \boldsymbol{k}_i)$, expressed as

$$U_i(\boldsymbol{g}; \boldsymbol{k}_i) = A\delta(\boldsymbol{g} - \boldsymbol{k}_i),$$ (S11)

and neglecting the propagation term ($z = 0$), we obtain a general expression where the scattered field appears as an interaction of the illumination field and the scattering potential, given as

$$U_s(\boldsymbol{k}; \boldsymbol{k}_i) = iA \frac{F(\boldsymbol{k} - \boldsymbol{k}_i)}{k_z}.$$ (S12)

The object spectrum or scattering potential is interrogated by the illumination field, represented by its wave vector $\boldsymbol{k}_i$. The scattering event results in a plane wave with an amplitude $\boldsymbol{U}_s(\boldsymbol{k}; \boldsymbol{k}_i)$, propagating along the direction $\boldsymbol{k}$.

Combined Multi-Plane Phase Retrieval and Super-Resolution Optical Fluctuation Imaging for 4D Cell Microscopy - Supplementary Material

1.2 Coherent Transfer Function

The microscope is modelled as a telecentric, diffraction limited optical imaging system. The microscope is fully characterized by the source spectrum and the illumination and detection Numerical Aperture (NA_{ill}, NA_{det}). Due to the limited bandwidth of our detection system (sCMOS camera), the intensity is described by a temporal average (denoted <>) of the interference between the scattered and un-scattered field and integrated over the source spectrum (ω) and the angular spectra (k_i, k).

$$I(x) = <\left| \int_{\omega, k_i, k} \left(U_i(x; \omega, k_i) + U_s(x; \omega, k_i, k) \right) \mathrm{d}k \mathrm{d}k_i \mathrm{d}\omega \right|^2 > . \tag{S13}$$

with $U_i(x; \omega, k_i) = A(\omega)e^{ixk_i}$ and $U_s(x; \omega, k_i, k) = iA(\omega)\frac{F(k-k_i)}{k_z}e^{ixk}$.

Developing the equation S13, we decompose the intensity into a sum of mutual intensities as

$$I(x) = < \int_{\omega', k_i'} \int_{\omega'', k_i''} U_i(x; \omega', k_i') U_i^*(x; \omega'', k_i'') \, \mathrm{d}\omega' \mathrm{d}k_i' \mathrm{d}\omega'' \mathrm{d}k_i'' > + \tag{S14}$$

$$< \int_{\omega', k_i', k'} \int_{\omega'', k_i''} U_s(x; \omega', k_i', k') U_i^*(x; \omega'', k_i'') \, \mathrm{d}\omega' \mathrm{d}k_i' \mathrm{d}k' \mathrm{d}\omega'' \mathrm{d}k_i'' > + c.c.$$

where $c.c.$ denotes the complex conjugate term $U_s^* U_i$. We neglected the weak $U_s U_s^*$ contribution due to the weak scattering approximation.

Using the generalized Wiener-Khintchine theorem[5], the mutual intensity of two fields is only non-zero for $\omega' = \omega''$. Following the work of N. Streibl[6], which applies for a telecentric configuration and a Koehler illumination, the mutual intensity is non-zero only for $k_i' = k_i''$. We then obtain

$$I(x) = \int_{\omega, k_i} U_i(x; \omega, k_i) U_i^*(x; \omega, k_i) \, \mathrm{d}\omega \mathrm{d}k_i + \tag{S15}$$

$$\int_{\omega, k_i, k} U_s(x; \omega, k_i, k) U_i^*(x; \omega, k_i) \mathrm{d}\omega \mathrm{d}k_i \mathrm{d}k + c.c.$$

The first term represents the unscattered field and the second term the mutual interference between the illumination and scattered fields.

The product between the scattered and un-scattered field contains all information of the object. Following equation (S11) and (S12), we obtain in the object Fourier space

$$U_s(g; \omega, k) \otimes U_i^*(g; \omega, k_i) =$$
$$iA(\omega)\frac{F(K; \omega)\delta(g-k)}{k_z} \otimes A^*(\omega)\delta(g+k_i) = iS(\omega)\frac{F(K; \omega)}{k_z}\delta(g-K), \tag{S16}$$

where $K = k - k_i$ (Laue equation) and $AA^* = S(\omega)$ the intensity of the light source. This expression is illustrated in Fig. S1a by the corresponding Ewald sphere construction taking into account the elastic light scattering. For a given frequency ω, illumination and scattering vector k_i and k, the scattering potential $F(g; \omega)$ at the spatial frequency K is interrogated with an amplitude $\frac{S(\omega)}{k_z}$.

Finally the interference term i.e. the cross-spectral density $\Gamma(g)$ is expressed

Combined Multi-Plane Phase Retrieval and Super-Resolution Optical Fluctuation Imaging for 4D Cell Microscopy - Supplementary Material

$$\Gamma(\boldsymbol{g}) = \int_{\omega, \boldsymbol{k}_i, \boldsymbol{k}} \mathrm{i} \frac{S(\omega)F(\boldsymbol{g};\omega)\delta(\boldsymbol{g}-\boldsymbol{K})}{k_z} \mathrm{d}\boldsymbol{k}_i \mathrm{d}\boldsymbol{k} \mathrm{d}\omega \qquad \text{(S17)}$$

where we integrate over the source spectra and the angular spectra (illumination and scattering).

Due to the limited bandwidth of our illumination, we neglect the dispersion of the scattering potential. This results in a linear relationship for the cross-spectral density.

$$\Gamma(\boldsymbol{g}) = \mathrm{i}F(\boldsymbol{g})H(\boldsymbol{g}) \qquad \text{(S18)}$$

with the polychromatic coherent transfer function $H(\boldsymbol{g})$,

$$\mathrm{H}(\boldsymbol{g}) = \int_{\omega, \boldsymbol{k}_i, \boldsymbol{k}} \frac{S(\omega)}{k_z} \delta(\boldsymbol{g}-\boldsymbol{K}) \mathrm{d}\boldsymbol{k}_i \mathrm{d}\boldsymbol{k} \mathrm{d}\omega. \qquad \text{(S19)}$$

Each combination of illumination and detection modes (frequency (ω) dependent) interrogates a different point of the object's spatial frequency content. The final transfer function is then given by a linear superposition of all contributions.

We obtained this result based on the Helmholtz equation using the first order Born approximation for describing the scattering field as an interaction between the illumination field and a weakly scattering object. The polychromatic illumination has been embedded in a generalized Wiener-Khintchine formalism. The spatial coherence is taken into account by a mutual intensity consideration following the seminal work of N. Streibl[6]. This work on 3D imaging is based on a telecentric configuration containing a Koehler illumination matching all experimental elements of our setup. As a main result of this analysis, the scattering potential $F(\boldsymbol{g})$ is low pass filtered by the imaging system as described by the Coherent Transfer Function (CTF) $H(\boldsymbol{g})$.

A key assumption we made to derive this linear model (equation (S18)) is the weak scattering approximation, i.e. only single scattering events contribute to the measured signal. This assumption is valid for example when imaging single layer of cells. Imaging thicker samples requires a modified theory taking into account multiple scattering events[1].

The complex ingredients of the theoretical analysis are illustrated in an Ewald sphere representation (Fig. S1b). For each wavelength, the Ewald sphere shows the frequency support which corresponds to an axially shifted sphere cap of radius $\bar{n}k_0$ with a lateral extent given by the product of the rescaled wave number k_0 with the detection numerical aperture ($g_{\perp max} = \bar{n}k_0 NA_{det}$) and an axial extent limited to[7]

$g_{z,\max}(g_\perp, NA_{det}) = \bar{n}g_\perp \left(1 - \sqrt{1 - \frac{NA_{det}^2}{\bar{n}^2}}\right)$. Each of these wavelength-dependent sphere caps are summed up to build the support of the polychromatic system transfer function, where the weights are given according to equation (S19).

Taking into account the full angular spectrum of the illumination, we integrate over all illumination $\boldsymbol{k}_i$. The resulting CTF $H(\boldsymbol{g})$ is shown in Fig. S1c.

Combined Multi-Plane Phase Retrieval and Super-Resolution Optical Fluctuation Imaging for 4D Cell Microscopy - Supplementary Material
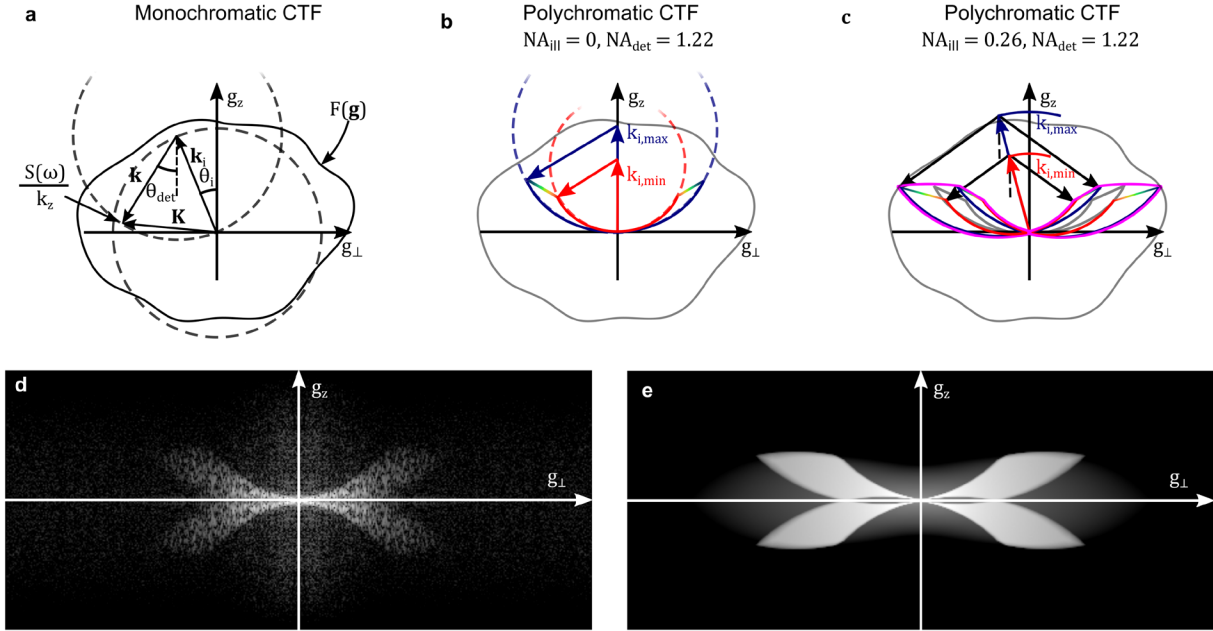

Figure S1 Construction of the polychromatic coherent transfer function. (a) Illustration of elastic light scattering (b) Frequency support of the polychromatic CTF with plane wave illumination, (c) Frequency support of the polychromatic CTF with Koehler illumination, (d) Logarithmic absolute valued 3D-FFT of experimental intensity stack, acquired by translating a sample of fixed hippocampal primary neurons in steps of 200 nm (≈50 μm x 50 μm x 40 μm), showing the system transfer function and its mirrored complex conjugate, (e) Logarithmic absolute valued 3D-FFT of simulated 3D intensity stack based on the proposed model ($NA_{ill} = 0.26, NA_{det} = 1.15$ source spectrum (Table S1)).

In complement to the theoretical analysis and the Ewald sphere representation, we calculate (Fig. S1d) the experimental 3D-fast Fourier Transform (FFT) of a large intensity stack, containing the transfer function $H(\boldsymbol{g})$ and its mirrored complex conjugate. Fig. S1e shows the simulated 3D-FFT of an equally large intensity stack, based on the experimental source spectrum, the illumination and detection NA.

2 Retrieving the complex 3D cross-spectral density $\Gamma(\boldsymbol{g})$

To recover the 3D cross-spectral density and its corresponding phase, only a 3D bright field image stack is required. The different planes can be acquired sequentially by a z-scan or in a multi-plane configuration (see Fig. S5), which provides camera rate 3D phase tomographic measurements. For each plane z_p we detect the interference of the incident field with the scattered field. Using equations (S15, S17), we write

$$I(\boldsymbol{x_p}) = I_{DC} + \Gamma(\boldsymbol{x_p}) + \Gamma^*(\boldsymbol{x_p}) \,, \tag{S20}$$

where we used the short-hand notation $\boldsymbol{x_p} = (x, y, z_p)$.

Taking the 3D Fourier transform of this equation, we obtain

$$I(\boldsymbol{g}) = I_{DC}\delta(\boldsymbol{g}) + \Gamma(\boldsymbol{g}) + \Gamma^*(-\boldsymbol{g}). \tag{S21}$$

Combined Multi-Plane Phase Retrieval and Super-Resolution Optical Fluctuation Imaging for 4D Cell Microscopy - Supplementary Material

The intensity spectrum can be decomposed into a DC-part $I_{DC}\delta(\boldsymbol{g})$ and an AC part, composed of two symmetric and conjugate cross-spectral densities. For small illumination NA, the cross-spectral density essentially expands into the subspace $g_z \geq 0$ (see Figure S1c,[3]). Both mirror-contributions $\Gamma(\boldsymbol{g})$ and $\Gamma^*(-\boldsymbol{g})$ of the scattering potential are largely dissociated.

Filtering the complex field $I(\boldsymbol{g})$

$$\Gamma_+(\boldsymbol{g}) = I(\boldsymbol{g})K(g_z) \tag{S22}$$

with a cutoff filter $K(g_z)$

$$K(g_z) = \begin{cases} 1 & if\ g_z > g_{z,c} \\ 0 & else \end{cases} \tag{S23}$$

suppresses both the conjugated cross-spectral density $\Gamma^*(-\boldsymbol{g})$ and the low frequency overlap.
This filtering condition entails the analyticity of the cross-spectral density along the axial direction i.e. the real and imaginary part of $\Gamma(x)$ form a Hilbert transform pair (Titchmarsh theorem)[8]. Therefore, the amplitude and the phase are simply two alternative representations of the filtered scattering potential, where the amplitude appears as the imaginary part of transfer function $H(\boldsymbol{g})$ and the phase as the real part of $H(\boldsymbol{g})$ (see S18). In other words, a point scatterer appears in intensity as an axial phase shift with no contrast in focus while the phase appears as a Gaussian with maximum contrast (see Fig. S3a).

The threshold $g_{z,c}$ is determined by the illumination NA (Fig. S1c). This translates directly to the suppression of the overlap of $\Gamma(\boldsymbol{g})$ and its mirrored complex conjugate $\Gamma^*(-\boldsymbol{g})$. The filter $K(g_z)$ acts as a high pass filter and removes this low frequency overlap.

We obtain for the cutoff

$$g_{z,c} = \bar{n}k_{0,max}\left(1 - \sqrt{1 - NA_{ill}^2}\right), \tag{S24}$$

where $k_{0,max} = \frac{2\pi}{\lambda_{min}}$. For our case with a $NA_{ill} \approx 0.26$ (coherence factor $s = \frac{NA_{ill}}{NA_{det}} = 0.21$), we suppress all frequencies $g_z < g_{z,c} \approx 0.4\ rad/\mu m$. Transformed into real space, it means that any axial structure larger than about $\frac{2\pi}{0.4} = 15\ \mu m$ will be suppressed. As we are interested in the scattering potential of a cell and its subcellular structure, this cutoff has no major impact on the image quality.

According to Born & Wolf[1], the radius of the coherence area for all the images shown is equal to $0.61\frac{\lambda_0}{NA_{ill}} = 1.36\ \mu m$, given the illumination NA and central wavelength $\lambda_0 = 0.58\ \mu m$. Measurements of objects larger than the coherence area are prone to be biased towards lower phase values. This lateral high-pass filtering is well-known in phase microscopy using partially coherent illumination[9].

Finally, it is important to notice that all the values discussed above are dependent on the numerical aperture of the illumination. Reducing the illumination NA will decrease the cutoff $g_{z,c}$, and similarly increase the coherence area, allowing accurate imaging of larger objects while being more sensitive to artefacts of coherent imaging.

Combined Multi-Plane Phase Retrieval and Super-Resolution Optical Fluctuation Imaging for 4D Cell Microscopy - Supplementary Material

2.1 Quantitative phase derivation

From a general point-of-view, the quantitative phase can be expressed as

$$\varphi(\boldsymbol{x}) = angle\left(\frac{U_s + U_i}{U_i}\right), \tag{S25}$$

where U_i is the reference field that would be measured without any sample and $U_s + U_i$ is the total field, including a sample. Hence, φ represents the phase delay due to the sample.

In order to link this expression to the cross-spectral density, we rearrange equation (S25)

$$\varphi(\boldsymbol{x}) = angle\left(1 + \alpha\frac{U_s}{U_i}\right) = \tan^{-1}\left(\frac{\alpha\left|\frac{U_s}{U_i}\right|\sin(\Delta\varphi)}{1 + \alpha\left|\frac{U_s}{U_i}\right|\cos(\Delta\varphi)}\right), \tag{S26}$$

which corresponds to the quantitative phase[10], with $\Delta\varphi = \varphi_s - \varphi_i$. It is important to note that equation (S25) applies to the object space. Since U_s and U_i have a different spatial frequency spectra, both fields will be filtered differently while propagating from the sample plane to the detector[11]. In order to account for this effect, we introduce a real positive calibration factor α which is experimentally determined using known and well-characterized technical samples (see Chapter 4).

Expanding the fraction by $\frac{|U_i|^2}{|U_i|^2}$, equation (S26) can be further simplified as ,

$$\varphi(\boldsymbol{x}) = \tan^{-1}\left(\frac{\alpha|U_i||U_s|\sin(\Delta\varphi)}{|U_i|^2 + \alpha|U_i||U_s|\cos(\Delta\varphi)}\right). \tag{S27}$$

Noting that $|U_i|^2$ is the mean intensity I_0, and $|U_i||U_s|\sin(\Delta\varphi)$ and $|U_i||U_s|\cos(\Delta\varphi)$ are equivalent to the imaginary and real part of $\Gamma_+(\boldsymbol{x})$ respectively, we obtain a general equation linking the quantitative phase to the cross-spectral density as,

$$\varphi(\boldsymbol{x}) = \tan^{-1}\left(\frac{\alpha\,Im\big(\Gamma_+(\boldsymbol{x})\big)}{I_0 + \alpha\,Re\big(\Gamma_+(\boldsymbol{x})\big)}\right). \tag{S28}$$

2.2 Quantitative phase algorithm

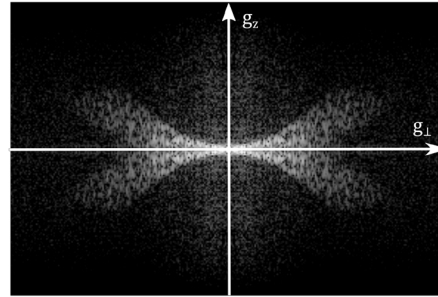The phase retrieval algorithm (see Fig. S2) can be summarized as follows
1. Data acquisition.
2. Signal mirroring along the axial direction to avoid boundary effects and 3D Fourier transform of the 3D stack.
3. Application of mask K for removing all $g_z \leq g_{z,c}$ contributions of the Fourier spectrum and Fourier denoising using a CTF-shaped mask.
4. Inverse Fourier transform for retrieving the cross spectral density in real space. Reconstruct the image field and calculate the 3D quantitative phase.

8

Combined Multi-Plane Phase Retrieval and Super-Resolution Optical Fluctuation Imaging for 4D Cell Microscopy - Supplementary Material
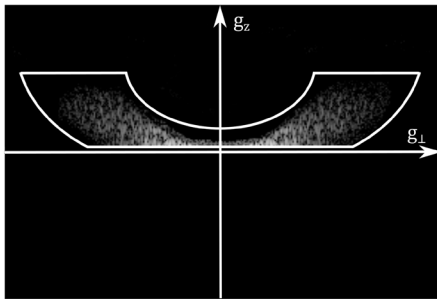
STEP 1: Data aquisition and multi-plane coregistration
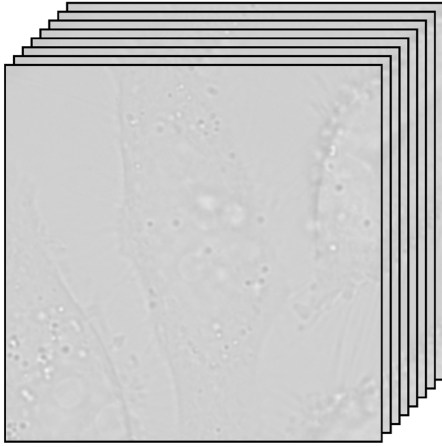
STEP 2: Signal mirroring and 3D FFT

STEP 4: i-FFT and phase calculation

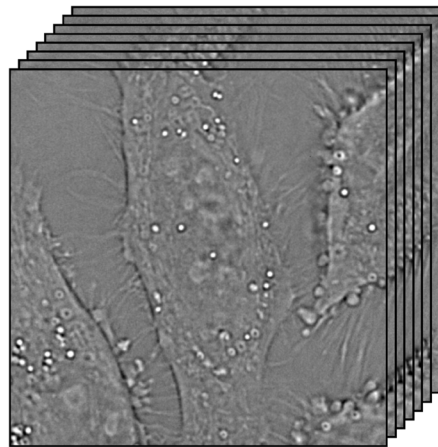**STEP 3: Fourier filtering and denoising**

Figure S2: Workflow of the phase retrieval algorithm. In STEP 1 and 4, 8-plane image stacks of fixed HeLa Cell are shown. In STEP 2 and 3, the data is displayed using a logarithmic scale.

3   Simulation and validation

3.1   Calculating the partially coherent system transfer function $H(\boldsymbol{g})$

For the illumination k-spectrum (limited by NA_{ill}), the corresponding Ewald sphere cap (limited by NA_{det}) is weighted according to the polychromatic spectrum of the source (Fig. S6) and projected on the reciprocal Fourier space (according to the specified field of view). These k-supports (Ewald sphere caps) are added to form the full polychromatic k-support. The calculated 2D CTF (basically a convolution of the illumination aperture and the detection aperture) is then mapped onto the 3D frequency support, taking into account the symmetry properties of the CTF (weighing according to equation (S16)), as shown in Fig. S1d.

3.2   3D image formation simulation

We define a point scatterer in real space by a Dirac function. The corresponding scattering potential is calculated and convolved with the previously established system transfer function $H(\boldsymbol{g})$ resulting in the complex 3D cross-spectral density $\Gamma(\boldsymbol{x})$. The 3D image intensity is given by the absolute squared

Combined Multi-Plane Phase Retrieval and Super-Resolution Optical Fluctuation Imaging for 4D Cell Microscopy - Supplementary Material

interference of the incident field with the scattered field (equation (S18)). All calculations have been performed using Matlab (R2016a).

3.3   Experiment vs simulation

We imaged 200 nm polystyrene beads sparsely distributed in agarose. Due to their size ($< \lambda/2$), we used the beads as an approximation of a point scatterer.

Fig S3a displays an axial cross-section of the computed and experimental 3D image (averaged over 15 individual measurements), showing an almost perfect match between experimental and simulated images. Their corresponding calculated phase underlines the validity of our model and is further demonstrated in lateral and axial line plots (Fig. S3b). Fig. S3c shows the color-coded maximal z-projection of the full experimental recovered phase stack. The orthogonal slice 1-2 shows the optical sectioning for our 3D phase imaging.
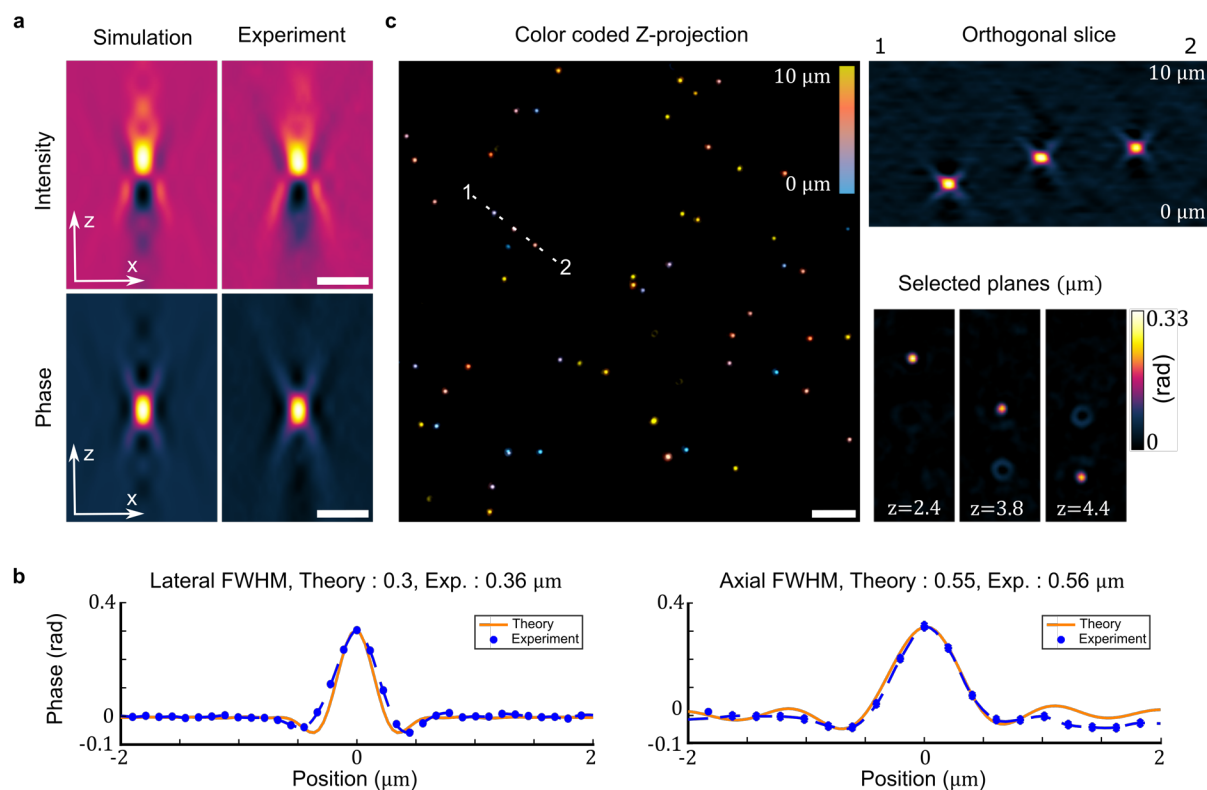

Figure S3 Experiments and simulations with polystyrene beads (a) 3D axial slice of computed and experimental (average over 15 measurements) intensity and phase of 200 nm polystyrene beads. Scale bar 1 µm, (b) Comparison of the theoretical and experimental phase profile showing almost perfect agreement, (c) Colour coded maximum z-projection of the phase of sparsely distributed beads. The orthogonal slice AB demonstrates the sectioning capability of the method. Scale bar 5 µm.

4   Quantitative phase calibration using technical sample

As discussed in Section 2, a calibration step is required to accommodate for the unequal transmission of the reference and the scattered fields.

Combined Multi-Plane Phase Retrieval and Super-Resolution Optical Fluctuation Imaging for 4D Cell Microscopy - Supplementary Material

In order to calibrate our analysis, we imaged a staircase-like nanometric structure made by repetitive chemical etching of a glass substrate (borosilicate, see Section 8.5). A total of 50 planes with an inter-plane distance of 200 nm were used to accurately extract the calibration factor. The in-focus bright field image and its corresponding calibrated phase are shown in Fig. S4a respectively Fig. S4b. Fig. S4c shows the Atomic Force Microscopy (AFM) measurement of the staircase structure used to calibrate the phase measurements. Due to the limited spatial coherence (same illumination aperture used for all imaging) which acts as a high-pass filter, only the edges can be quantitatively resolved in the phase image.

The AFM measurements allow to compute the theoretical phase signal as $\varphi = k_0 \, \Delta n \, h$, where $k_0 = \frac{2\pi}{\lambda} = 10.8 \; \mu m^{-1}$, $\Delta n = n_{glass} - n_{air} = 1.51 - 1$ in air and h is the relative step height. The calibration factor is then estimated by solving equation (S28) for α and using the expected theoretical phase and the measured imaginary and real parts of the cross-spectral density, and the average intensity. For our setup, we estimated $\alpha = 3.15$. The Fig. S4d shows calibrated phase and AFM line plots demonstrating how the phase signal varies proportionally to the step height. The Fig. S4e shows (orange dots) all the recovered phase jumps of the 6 steps (Fig. S4c).
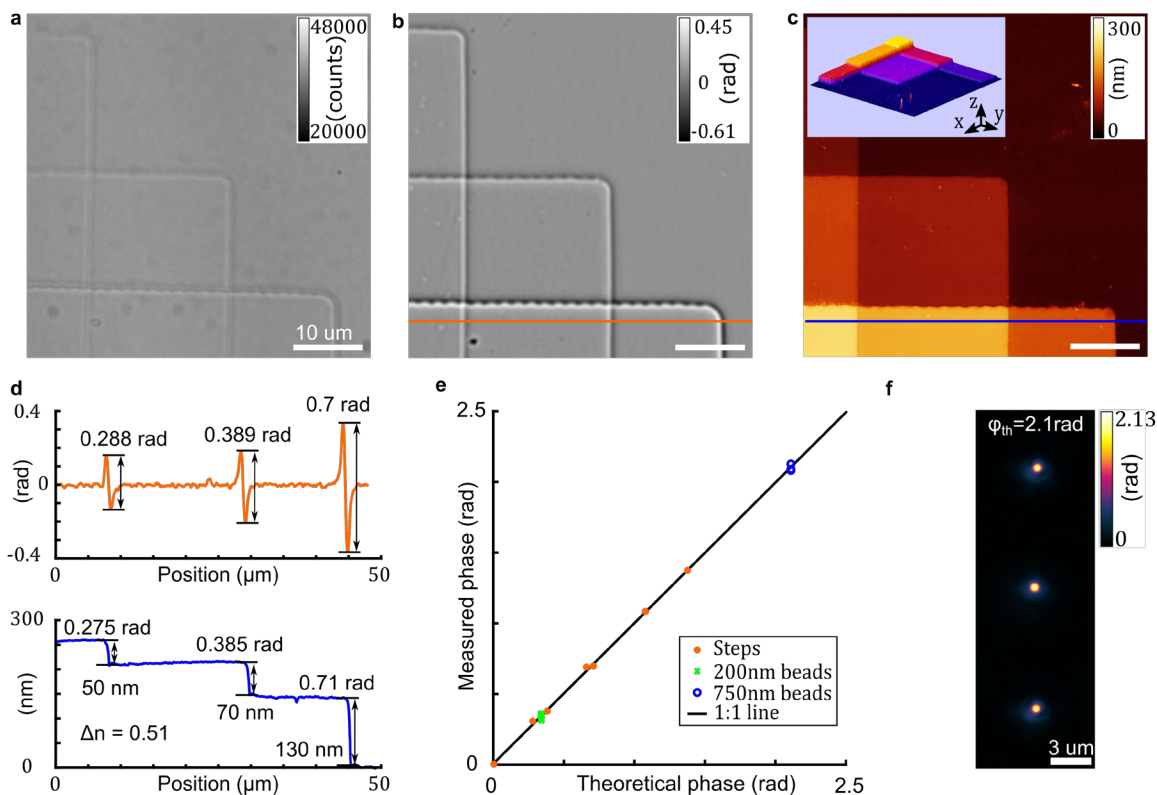

Figure S4 Quantitative phase imaging of technical sample. (a) In-focus bright field image of nanometric step like borosilicate structure, (b) Corresponding quantitative phase after processing of the intensity stack, (c) AFM measurement (insert : 3D surface plot using ImageJ[12]), (d) Line plots of selected lines indicated in (b) and (c), quantitative phase (orange), AFM measurement (blue), (e) Measured phase vs. theoretical phase for step heights (orange dots), 200 nm polystyrene beads (green cross) and 750 polystyrene beads (blue circle). The 1:1 line is also plotted to provide a visual reference, (f) Max. phase projection of 750 nm polystyrene beads.

Combined Multi-Plane Phase Retrieval and Super-Resolution Optical Fluctuation Imaging for 4D Cell Microscopy - Supplementary Material

In order to validate the calibration, we imaged 200 nm and 750 nm polystyrene beads ($n_{beads} = 1.59$) embedded in agarose $(n_{agar} = 1.33)$, for a total of 50 planes with an inter-plane distance of 200 nm (shown in Fig. S3). The obtained phases are in total agreement with the theory. The 200 nm beads being smaller than the system point-spread function, the theoretical phase has to be adjusted by averaging the optical path length over the beads diameter which provides an estimated correction factor of ≈ 0.6, leading to a theoretical phase shift of 0.34 $[rad]$. We measured an average phase of 0.33 ± 0.014 [rad] (average over 15 beads, depicted as a green crosses in Fig. S4e). The 750 nm beads being larger than the phase point-spread function, we only have to consider the maximal phase shift. Fig. S4f shows the maximal phase projection of 750 nm beads, providing another independent confirmation of the ability of the method to achieve quantitative phase imaging (theoretical phase of 2.106 $[rad]$ and average measured phase of 2.08 $[rad]$).

5   Fourier space sampling

From a practical point-of-view, the quality of our phase retrieval method depends on two main parameters: the inter-plane distance and the total number of planes used for imaging. The inter-plane distance Δz is directly related to the Nyquist-Shannon sampling theorem[13]. The number of planes determines how well one can filter the overlap between Γ_+ and Γ_-.

In detail, for a given number of plane, the Fourier sampling step is given by $\Delta g_z = \frac{\pi}{(N_{planes}-1)\Delta z}$. Reducing the number of plane results in a coarser sampling of the Fourier space. As a consequence, some useful signal is mixed with the overlap region, ultimately resulting in a lateral high-pass digital filtering of the quantitative phase. This restriction can also be seen in real space where reducing the number of plane limits the ability to acquire defocused images. Since large objects do not scatter light with high angles, the limited axial sampling is not able to measure the slow variations of intensity.

We illustrate in Fig. S5a,b the impact on the phase retrieval when taking $N_{planes} = 3$, 8 or 18 z-planes (scanning inter-plane distance of $\Delta z = 350\ nm$).

The minimal number of planes required for optimal removal of the overlap contribution (that is when the axial sampling of the CTF matches the maximal axial frequency of the overlap) can be easily estimated from a Fourier sampling analysis and correspond to the case where the sampling step Δg_z is equal to the cutoff frequency $g_{z,c}$. A simple estimation supposing a $\Delta z = 350\ nm$ and the cutoff limit for suppressing the overlap ($NA_{ill} \approx 0.26$, $k_{0,max} = \frac{2\pi}{\lambda_{min}} = 11.5\ rad/\mu m$, equation (S24)) results in

$$N_{planes} = 1 + \frac{\pi}{\Delta z\ g_{z,c}} \approx 18\ planes \qquad (S29)$$

We provide the reader equation (S29) as a simple tool to estimate the number of planes required to achieve high-quality phase reconstruction for a given sampling step Δz, illumination NA and source spectrum (which both influence the term $g_{z,c}$).

12

Combined Multi-Plane Phase Retrieval and Super-Resolution Optical Fluctuation Imaging for 4D Cell Microscopy - Supplementary Material
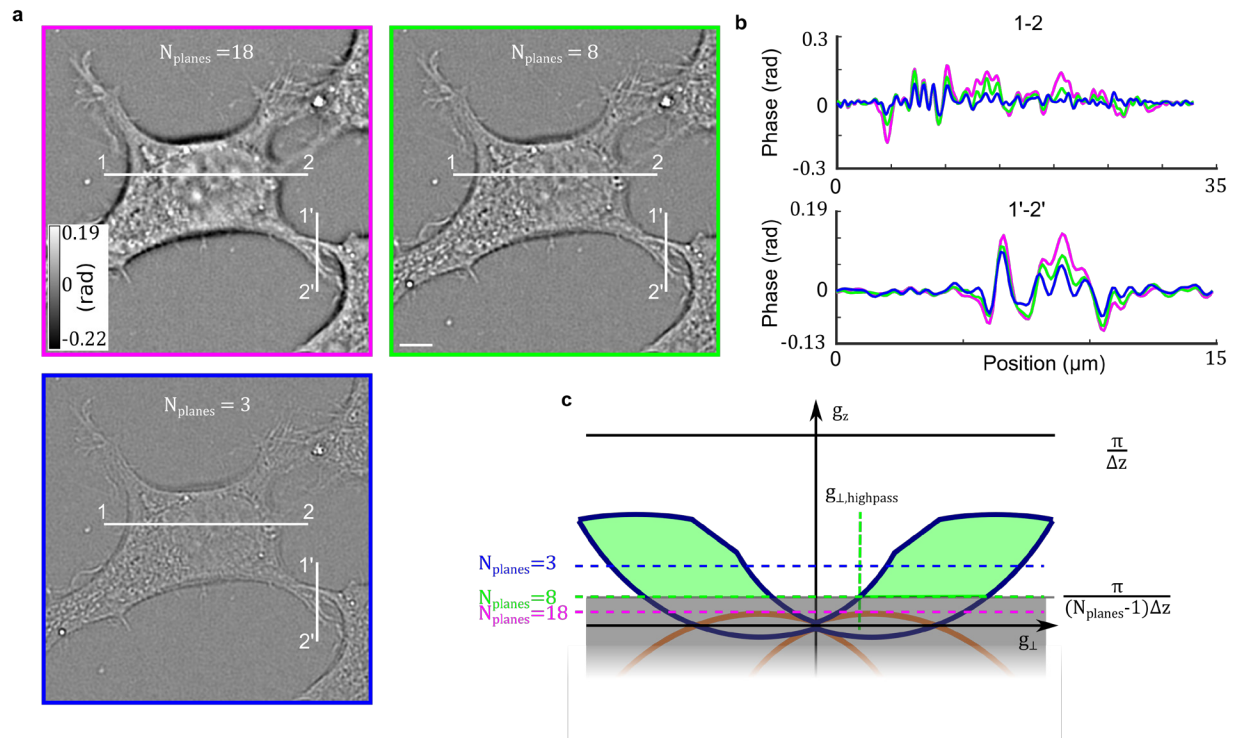

Figure S5: Influence of the number of planes on phase reconstruction (a) N_{planes} = 18,8,3 plane reconstructions of a fixed HeLa cell imaged with an inter-plane distance of $\Delta z = 350\,nm$ (magenta, green and blue), highlighting the high-pass filtering imposed by the sampling. By increasing the number of planes, larger structures are clearly revealed (b), Line plots along perpendicular directions indicated in (a) for phase reconstructions with three different samplings showing the consistency of the recovered phase, (c) Theoretical representation of the transfer function $H(\boldsymbol{g})$ showing how the inter-plane distance and the number of planes limits the accessible frequency space. The indicated N_{planes}=3,8,18 dotted-lines illustrate the lower accessible g_z limit. The accessible spatial frequency space for the 8 planes is highlighted in green. Scale bar 5 μm.

The high-pass filtering side-effect of limited axial Fourier sampling can be easily seen in Fig. S5c (intersection of the horizontal line Δg_z with the transfer function footprint), and the lateral cutoff frequency can be expressed as

$$g_{\perp,highpass} = -rNA_{ill} + \sqrt{r^2 - \left[\Delta g_z - r\sqrt{1 - NA_{ill}^2}\right]^2},$$ (S30)

where $r = \bar{n}k_{0,min}$ is the radius of the smallest Ewald sphere (see Chapter 2) and Δg_z is the axial sampling step. In our case (8 planes), we estimate $g_{\perp,highpass} \approx 4.6\,rad/\mu m$. Converted in real space, this means that any objects larger than $\approx 1.4\,\mu m$ will be filtered out. This effect can be seen for phase imaging of a HeLa cell in Fig. S5a,b. The coherence area diameter (2.72 μm, see Section 2) is larger than the 1.4 μm limit due to spatial filtering in our 8 plane configuration. Therefore, the spatial frequency content that passes through the digital filter can be used for quantitative phase imaging.

The imaging of 200 nm polystyrene beads using the prism (8 planes) confirmed the quantitativeness of the method. We measured an average phase of 0.33 rad ($\varphi_{th} \approx 0.34\,rad$).

If the quantitative phase of larger objects (up to the spatial coherence diameter) is of interest, more planes could be used. Indeed, in the ideal sampling case, the digital filtering cut-off (for 18 planes ≈

13

Combined Multi-Plane Phase Retrieval and Super-Resolution Optical Fluctuation Imaging for 4D Cell Microscopy - Supplementary Material

5 µm) is much less severe than the limit due to spatial coherence. Hence, the size of the largest object that can be imaged quantitatively is ultimately only limited by the spatial coherence area.

Here, we used 8 planes as a reasonable compromise between the speed, the low-frequencies recovery and the ability to combine our novel quantitative phase imaging with 3D Super-resolution Optical Fluctuation Imaging (SOFI).

6 PRISM multi-plane platform for 3D phase and SOFI imaging

The telecentric multi-plane platform (MP) allows the simultaneous acquisition of 8 fluorescence or bright field images originating from 8 object planes with a constant inter-plane distance (Fig. S6). The fluorescence excitation is realized by wide-field epi-illumination, whereas phase imaging uses the Koehler bright field arm from a commercial Zeiss microscope. The detection system is common to both imaging modalities, i.e., the setup is a classical microscope with an integrated telescope containing an image splitting prism in the detection path (optical design (Section 6.3) and specification LOB-EPFL, Lausanne; manufacturing Schott SA, Yverdon, Switzerland). An adjustable field stop in the intermediate image plane prevents the overlap of the images on the cameras. All lenses and optomechanics are standard commercial components, except for the custom-made holder for the prism and cameras (see Figure S7 and Table S1 for the list of optical components). This versatile MP microscope allows diffraction limited imaging for all 8 conjugated object-image planes.

14

Combined Multi-Plane Phase Retrieval and Super-Resolution Optical Fluctuation Imaging for 4D Cell Microscopy - Supplementary Material
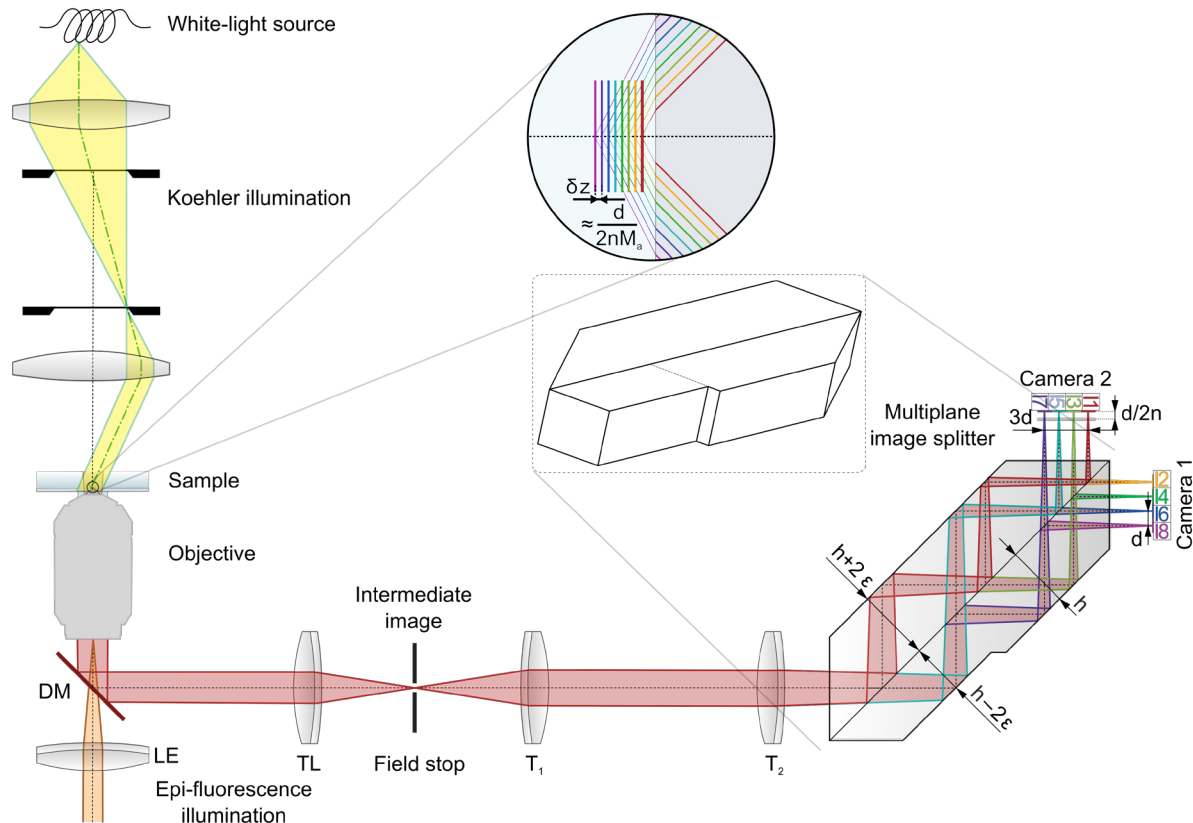

Figure S6. Microscope setup. Wide-field epi-illumination for fluorescence imaging combined with a Koehler trans-illumination for phase imaging. The multi-plane image splitting prism directs the light coming from 8 axially distinct planes in the sample towards 4 adjacent fields of view on each of the two cameras. The lenses in the detection path are arranged as a sequence of four 2f configurations. DM dichroic mirror, LE lens, TL tube lens, T_1 and T_2 lenses.

Component	Specifications
White light Koehler illumination	Axiovert 100 M, 12 V 100 W Halogen lamp (Carl Zeiss)
Fluorescence widefield epi-illumination	120 mW, 405 nm laser (iBeam smart, Toptica)
	800 mW, 635 nm laser (MLL-III-635, Roithner Lasertechnik)
	800 mW, 532 nm laser (MLL-FN-532, Roithner Lasertechnik)
Objective	UPLSAPO 60XW 1.2 NA (Olympus)
Microscope stage	piezoLEGS® stage (3-PT-60-F2,5/5) and Motion-Commander-Piezo controller (Nanos Instruments GmbH)
Filters	Dichroic zt405/488/532/640rpc, (Chroma)
	Emission filters adapted to the respective experiment
Tube lens	$f_{TL} = 140\ mm$ (achromatic doublet G036-146-000 (AC 140/22.4, ANR 574070), Qioptiq)
Telescope lenses	$f_{T_1} = 160\ mm$ and $f_{T_2} = 200\ mm$ (achromatic doublets G630-631-660 (AC 160/22.4, ANR 576447) and G063-148-000 (AC 200/22.4, ANR 556031), Qioptiq)
Prism	Corning C-7980, n= 1.458 (at 587.56 nm), Abbe number V = 67.8
	See Section 6.2
Camera	Orca Flash 4.0 (Hamamatsu), pixel pitch $P_{Camera} = 6.5\mu m$

Table S1.Components of the MP detection. All optomechanics are standard commercial components, except for the custom-made holder for the prisms and cameras.

Combined Multi-Plane Phase Retrieval and Super-Resolution Optical Fluctuation Imaging for 4D Cell Microscopy - Supplementary Material
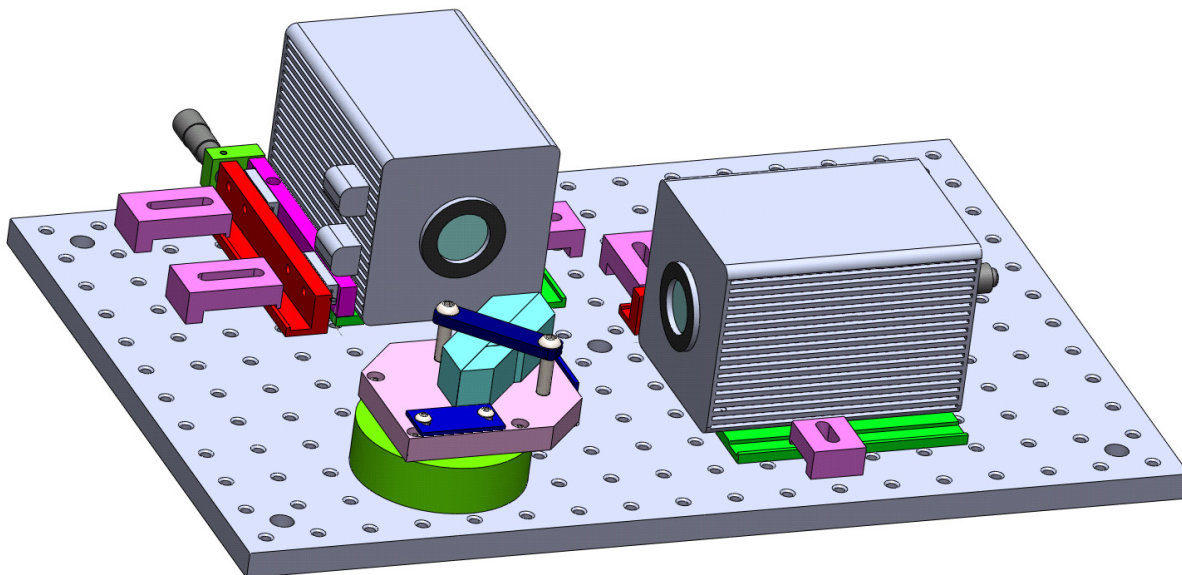

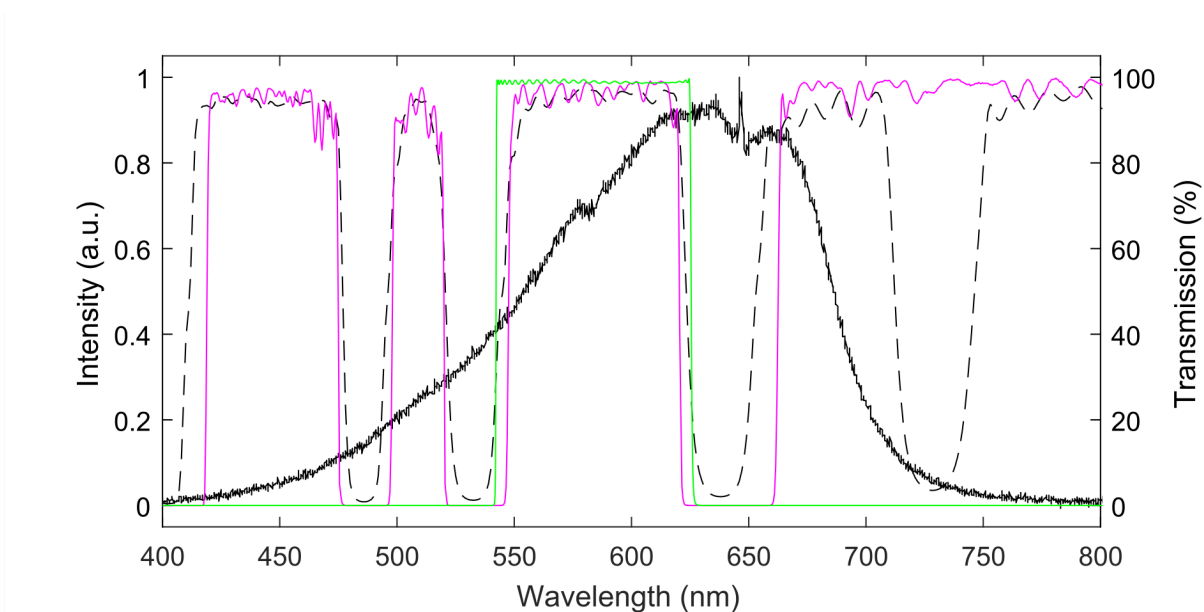Figure S7. Custom-made holder for the prism and cameras.

Figure S8. Spectrum of the white-light source and filter set. The spectrum of the halogen lamp (black line) was measured at 4 V drive voltage with a fibre-coupled spectrometer (CCS200M, Thorlabs). The transmission window(s) of the filters are indicated. Dichroic ZT 405/488/532/640/730rpc (dashed black, Chroma), emission filter Bright Line 582/75 (green, Semrock) and quad band emission filter ZET 405/488/532/640m (magenta, Chroma).

Combined Multi-Plane Phase Retrieval and Super-Resolution Optical Fluctuation Imaging for 4D Cell Microscopy - Supplementary Material

6.1 ABCD description of the MP detection

Fig. S9 shows the overall MP concept along with a basic ABCD matrix description for the system. All optical distances are chosen at the corresponding focal length per element such to ensure telecentricity in the object and image spaces. The intermediate image contains the field stop, which prevents overlap between the images at the detector plane(s). The multi-plane image splitter is located in the convergent path and introduces both a lateral offset and an axial path length difference among the image fields. Each object plane has its corresponding conjugated image plane. The overall lateral magnification of the platform is that of the classical microscope combined with a telescope $M_l = M_{Mic}M_{tel} = \frac{f_{TL}f_{T_2}}{f_{Objective}f_{T_1}}$.

For this study, we chose a 60× water-immersion objective and lenses as indicated in Table S1. Altogether, this amounts to a lateral magnification of $M_l \approx 58.3$ which results in a back-projected pixel size $p = \frac{P_{Camera}}{M_l} \approx 111\ nm$.
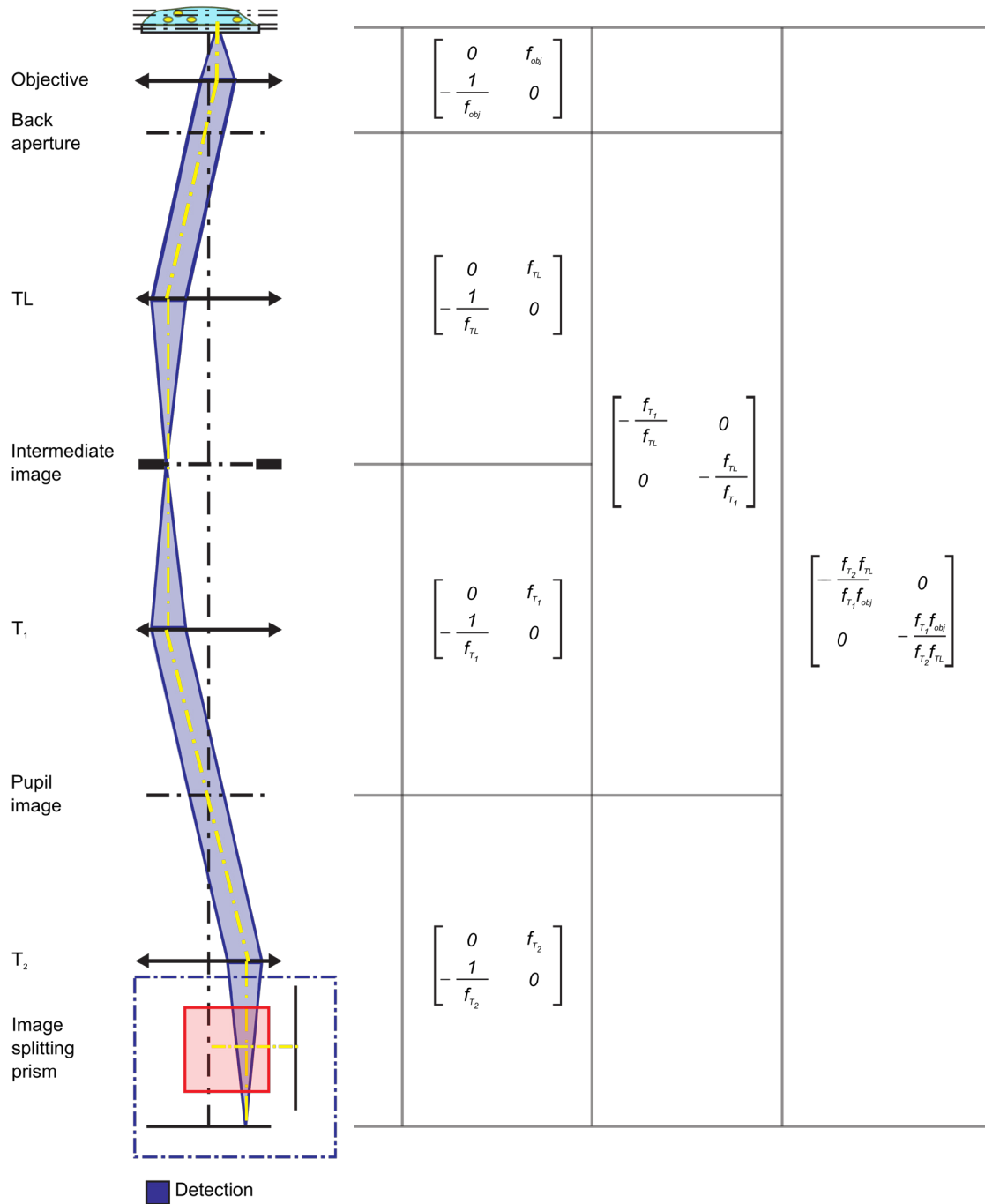
Figure S9. ABCD description of the MP concept. The full system can be decomposed into 4 distinct 2f systems. The scheme shows the system as an object- and image-side telecentric system. The TL-T$_1$ system is a telescope, mapping the back focal plane of the objective into the pupil plane. We use the convention $\begin{bmatrix} h \\ \alpha \end{bmatrix}$ with the ray height h and ray angle α.

Combined Multi-Plane Phase Retrieval and Super-Resolution Optical Fluctuation Imaging for 4D Cell Microscopy - Supplementary Material

6.2   Image splitter prism design

As shown in Fig. S6 and S10, the image splitter consists of 3 individual prisms glued along the common interfaces. The different images have individual paths and accumulate path length differences such that a conjugated object-image condition is ensured. The light paths undergo multiple total reflection at the outer prism interfaces, whereas the common inner interface has a customized 50:50 coating for equal image intensities.
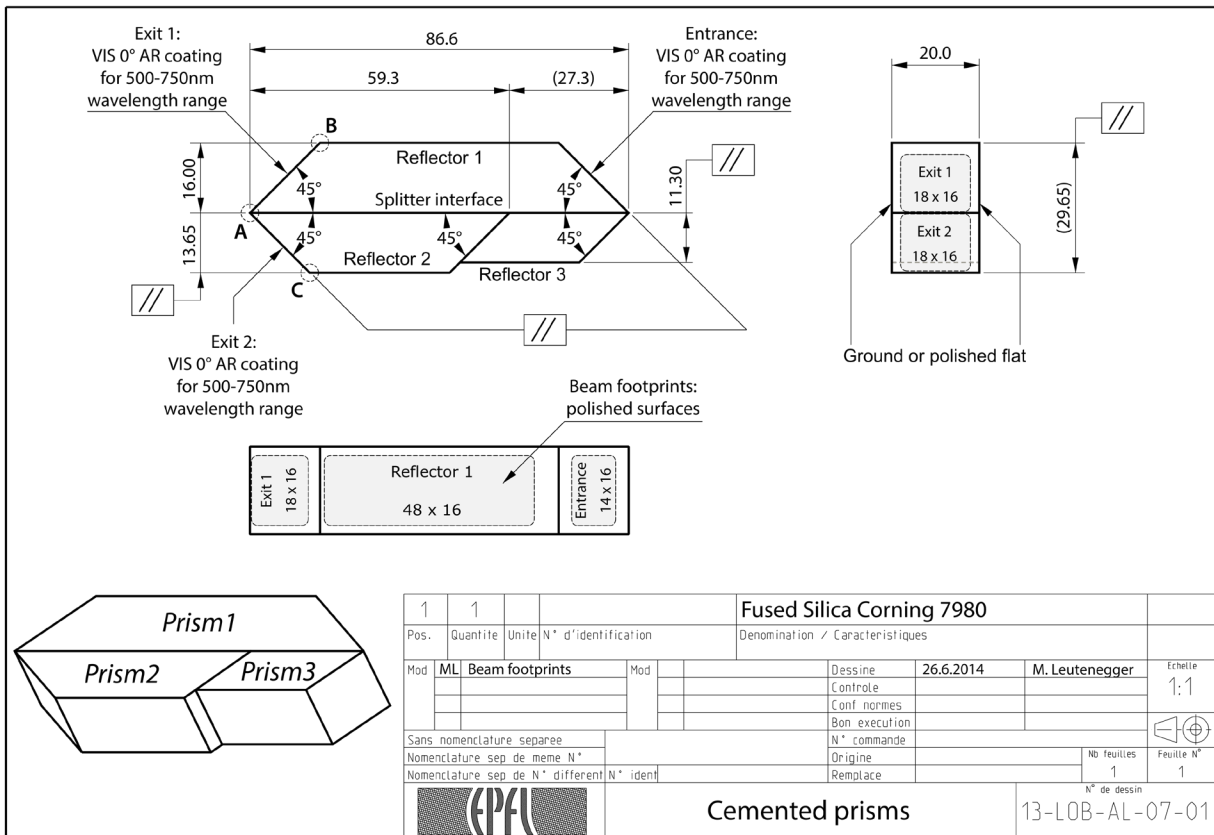

Figure S10. Technical drawing of the image splitter prism assembly.

Essential for a constant inter-plane distance and a constant lateral displacement d are the different prism heights h and $h \pm 2\varepsilon$ ($\varepsilon = \frac{d}{\sqrt{2}}$). As indicated in Fig. S6, the images are channelled in an interlaced fashion, i.e. the odd images (1, 3, 5, 7) are acquired by camera 1, the even images (2, 4, 6, 8) are acquired by camera 2. The neighbouring images on both cameras are laterally displaced by a distance d, which corresponds to a path length difference of $\Delta z = \frac{d}{n}$ (prism refractive index n = 1.458), i.e. for example the path length difference of image 7 to image 5 equals Δz. The first camera is additionally shifted by $\Delta z_{IP} = \frac{d}{2n}$, which results in a constant inter-plane (IP) distance of the consecutive axial planes Δz_{IP}. We chose the displacement of neighboring images $d = 3.32$ mm such that the row of four images matches the width of the sCMOS sensor (Orca Flash 4.0, Hamamatsu). The geometric path lengths of the rays in the prism range from 96.52 mm for the images 7 and 8 to 106.48 mm for the images 1 and 2. We performed an analysis of image aberrations using Zemax. Results are summarized in Section 6.3 below.

Combined Multi-Plane Phase Retrieval and Super-Resolution Optical Fluctuation Imaging for 4D Cell Microscopy - Supplementary Material

The inter-plane distance of consecutive axial planes in object space is then given by $\delta z_{IP} = \frac{\Delta z_{IP}}{M_a}$ where $M_a = M_l^2$ is the axial magnification. Experimentally, the inter-plane distance was estimated as 347 ± 11 nm (mean $\pm$ standard deviation of 8 individual measurements of surface immobilized fluorescent beads scanned along the optical axis in 200 nm steps).

6.3   Analysis of the MP design performance

The overall system has been fully designed based on ray tracing with Zemax (Radiant Zemax LLC). The layout of the optical design of the detection path is shown in Fig. S6. As we are lacking the objective's design data, we modelled the objective as a paraxial lens with 3 mm focal length and 7.2 mm aperture diameter. The field stop is adjusted to suppress crosstalk between the different images, resulting in an image side numerical aperture of $NA_i = 0.031$. All lenses (TL, T_1, T_2) are in this paraxial path and are standard lenses (Qioptiq) as indicated in Table S1. All optical distances are chosen at the effective focal length per element (see Fig. S11). The objective is placed in a telecentric configuration and the tube lens TL to the image plane is almost image-side telecentric (exit pupil position > 33 m from the image plane).
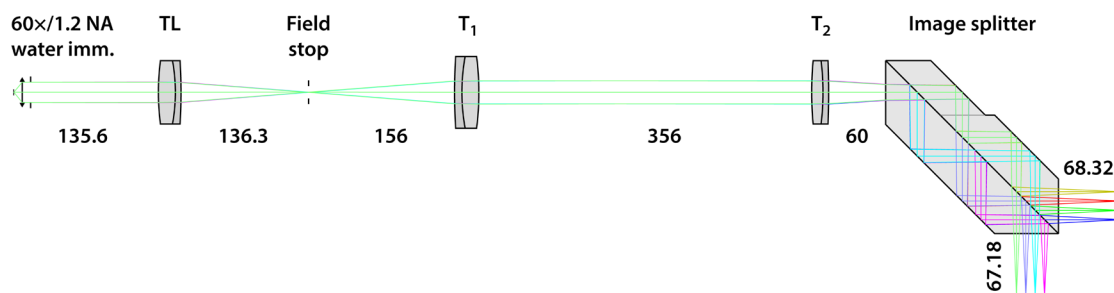

Figure S11. Layout of the detection system containing a 60×/1.20 NA water immersion objective, the tube lens ($f_{TL} = 140$ mm), the field stop, the telescope lenses T_1 ($f_1 = 160$ mm) and T_2 ($f_2 = 200$ mm) and the image splitter with two cameras. The free-space distances are indicated in millimetres and are 3x downscaled in the Figure.
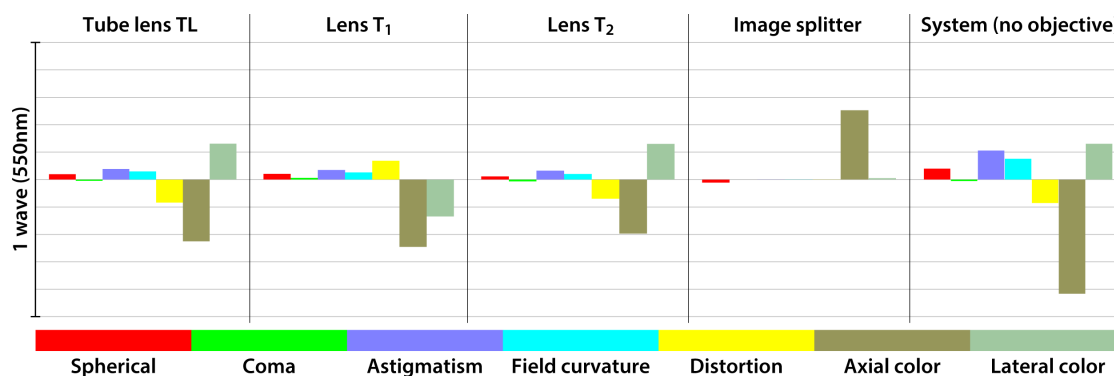

Figure S12. Seidel diagram (third-order aberrations) of the detection path. The major aberrations of the system are axial colour with about 0.4 waves, and lateral colour and astigmatism with about 0.1 waves each.

Our analysis of the optical aberrations based on the Seidel diagram (Fig. S12) shows that the spherical aberration due to the prism is insignificant. Moreover, the axial colour (chromatic length aberration, CLA) of the prism compensates the axial colour of all lenses. Therefore, the remaining system aberrations are due to the "unknown" aberrations of the objective and the residual aberrations of the lenses. The Seidel diagram shows that the axial colour is the dominant aberration with CLA < λ/2 in the

20

Combined Multi-Plane Phase Retrieval and Super-Resolution Optical Fluctuation Imaging for 4D Cell Microscopy - Supplementary Material

wavelength range 500–650 nm. These residual aberrations are even lower for the used wavelength range. The optical path length differences (OPD) are below $\lambda/2$ for the wavelength range and field sizes up to 100 µm in diameter (Fig. S13). For all fields and wavelengths, the geometrical PSF is below the Airy radius indicating clearly a diffraction-limited performance (Fig. S14). As shown in the spot diagrams, the chief ray positions shift slightly due to lateral chromatic aberration well below the Airy radius, indicating that these residual lateral chromatic aberrations are insignificant. The diffraction-limited performance of the detection system is also evidenced by the polychromatic modulation transfer and point spread functions (Fig. S15), showing a Strehl ratio > 0.95.

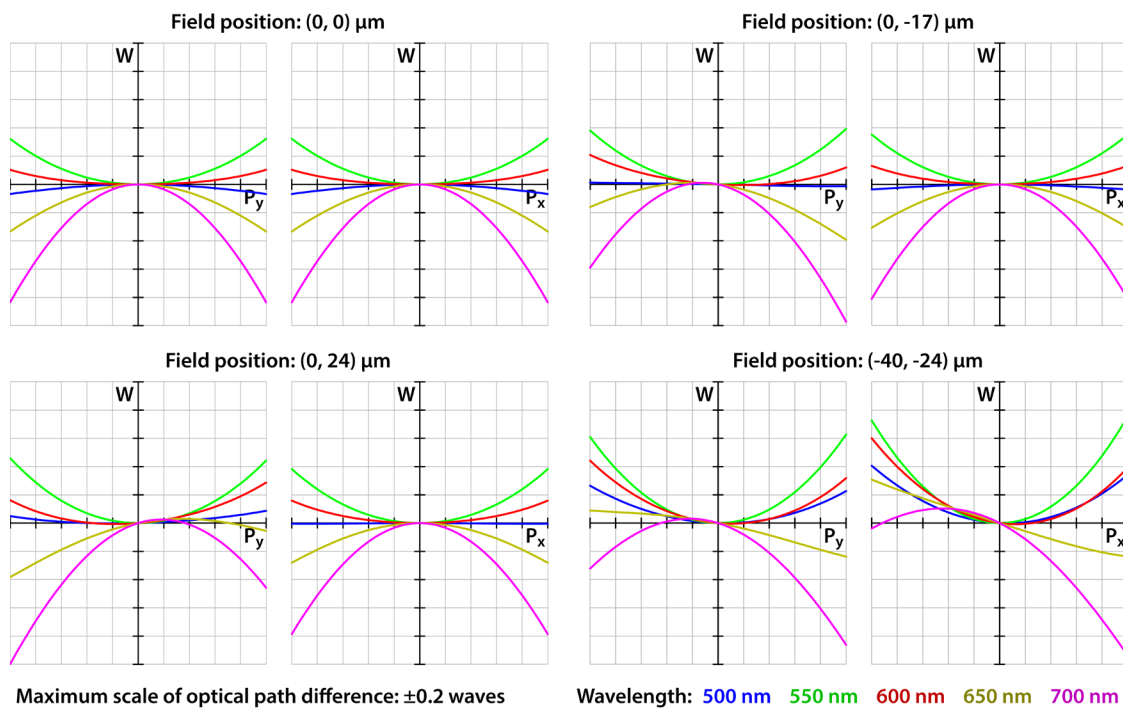In summary we have a diffraction limited performance of our MP system.

Figure S13. Optical path length difference (OPD) versus normalized pupil position. The OPD shows diffraction-limited performance ($|W| < 0.2$ waves) over an extended wavelength range and field.
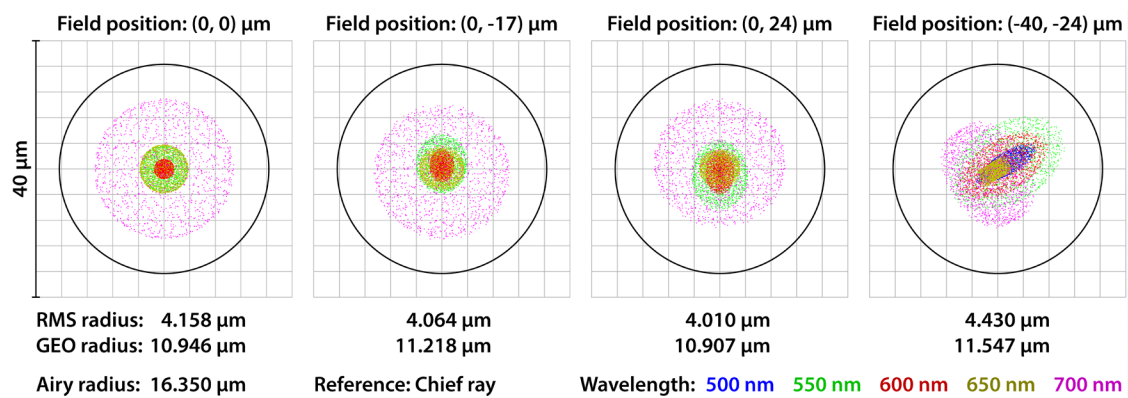

Figure S14. Spot diagrams of the ray intersections in all image planes. The root-mean-square (RMS) radii of the spots are much smaller than the Airy radius, which confirms the diffraction-limited performance across all image fields.

Combined Multi-Plane Phase Retrieval and Super-Resolution Optical Fluctuation Imaging for 4D Cell Microscopy - Supplementary Material
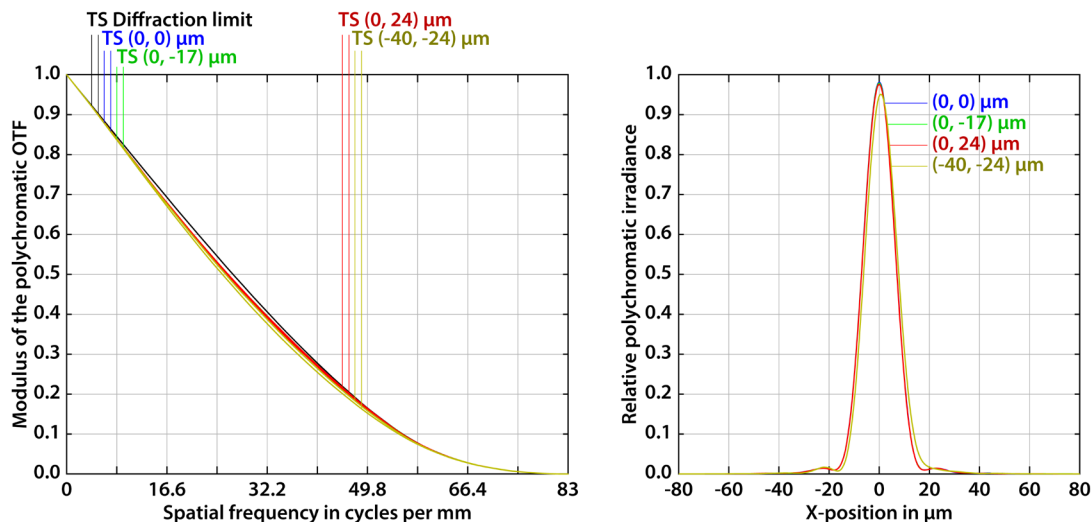

Figure S15. Polychromatic modulation transfer function (MTF) and point spread function (PSF). The MTF closely approaches the diffraction limit for all field positions and the PSF peak value and the Strehl ratio – are well above 0.8.

6.4   MP prism calibration

3D multi-plane imaging demands accurate calibration of the image planes. Co-alignment for both imaging modalities is based on an affine transformation and bilinear image interpolation (see Fig. S16). The transformation parameters are extracted from a calibration measurement of fluorescent beads scanned along the optical axis in 200 nm steps over the whole sampling volume.

The beads calibration measurements are also used to correct the transmission variation among the 8 image channels (slight deviation from 50:50 channel splitting) for SOFI processing. For phase imaging, the channels transmission correction is based on bright field images.
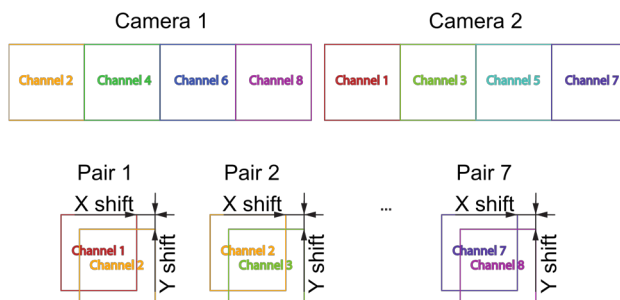

Figure S16. Co-registration of image planes.   An affine transformation and bilinear interpolation based on a calibration measurement with fluorescent beads is applied to (pairs of) image channels at different steps in the analysis routine.

22

Combined Multi-Plane Phase Retrieval and Super-Resolution Optical Fluctuation Imaging for 4D Cell Microscopy - Supplementary Material

7   Workflow - MP SOFI analysis

Fig. S11 shows the MP SOFI analysis workflow step by step.

1. Acquisition of raw images followed by image processing in subsequences. This avoids bleaching induced correlations over the full raw image sequence[14–16].
2. 3D Cumulant analysis at zero-time lag in a sliding bi-plane configuration for minimizing interpolation induced noise; Bi-plane cumulant block co-alignment.
3. Cumulant flattening, deconvolution and linearization followed by subsequence linear combination[17,18].
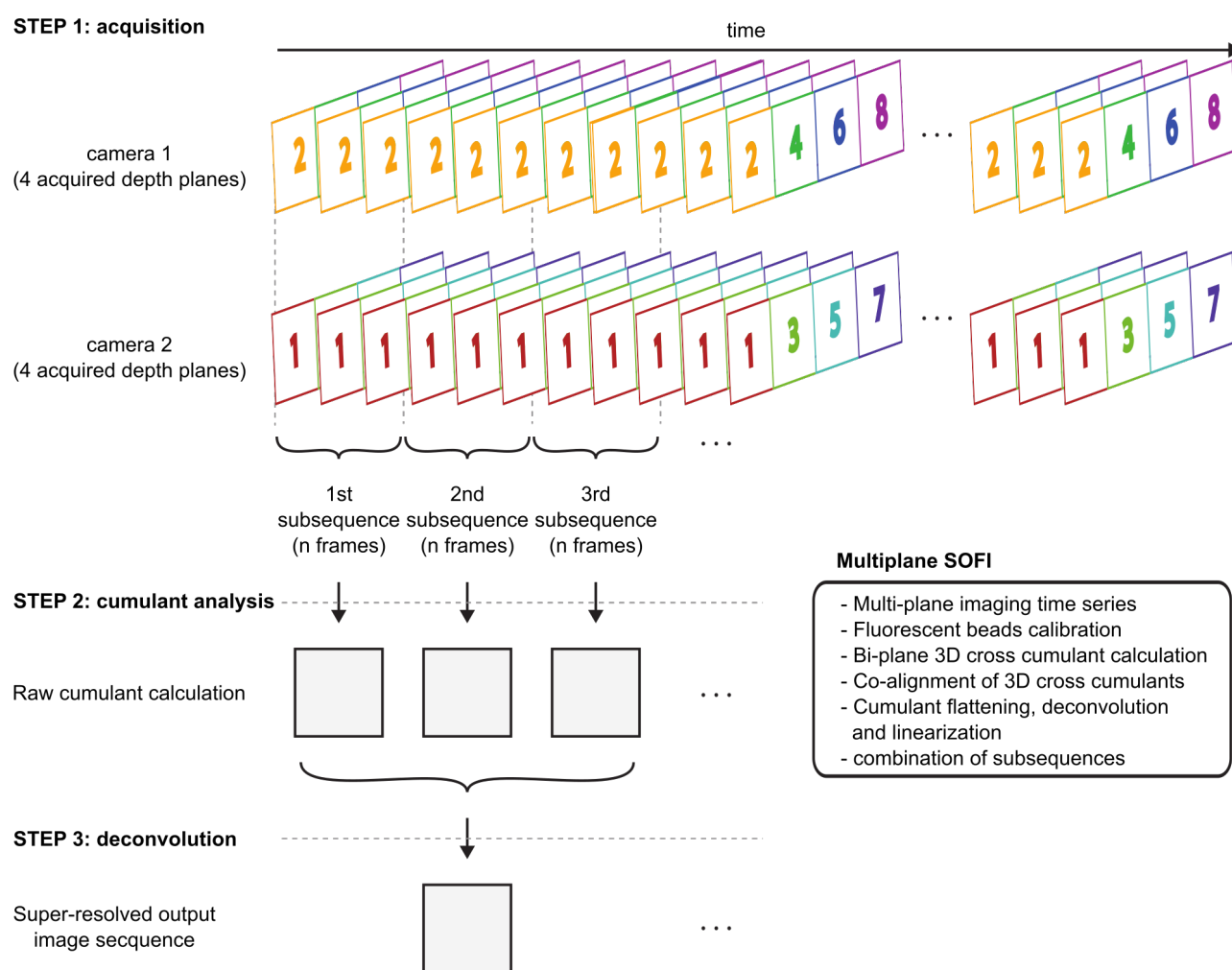
More details about the algorithm can be found in [14].

Figure S17. Workflow MP SOFI analysis.

Combined Multi-Plane Phase Retrieval and Super-Resolution Optical Fluctuation Imaging for 4D Cell Microscopy - Supplementary Material

8   Experiments

8.1   Imaging and Analysis Parameters

Experiment	Figure	Imaging mode	Excitation intensities[a]	Filter	Total # frames	Inter-plane distance	Frame rate[e]	Total movie acquisition time
HeLa cell fixed, unlabelled	Fig. 2, Fig. S4	phase	4 V halogen lamp	Bright Line 582/75[c]	50[d]	200 nm	20 ms	N/A
Human fibroblast cells live, unlabelled	Fig. 4	phase	4 V halogen lamp	Bright Line 582/75[c]	5000	350 nm	200 Hz	25 s
HeLa cell – Alexa Fluor 647 immunolabelled microtubules	Fig. 5	SOFI	<2 kW cm^{-2} at 635 nm 7 W cm^{-2} at 405 nm	ZET405/488 /532/640m[b]	5000	350 nm	50 Hz	100 s
		phase	4 V halogen lamp		1	350 nm	20 ms	N/A
primary hippocampal neuron – Alexa Fluor 647 immunolabelled α –synuclein aggregates	Fig. 5	SOFI	<2 kW cm^{-2} at 635 nm 7 W cm^{-2} at 405 nm	ZET405/488 /532/640m[b]	5000	350 nm	50 Hz	100 s
		phase	4 V halogen lamp		1	350 nm	20 ms	N/A
RAW 264.7 cells expressing Lifeact-Dreiklang	Fig. 5	SOFI	800 W cm^{-2} at 532 nm 8.5 W cm^{-2} at 405 nm	Bright Line 582/75[c]	3000	350 nm	50 Hz	60 s
		phase	4 V halogen lamp		1	350 nm	20 ms	N/A
primary hippocampal neuron – Alexa Fluor 647 immunolabelled α –synuclein aggregates	Fig S1	phase	4 V halogen lamp	Bright Line 582/75[c]	200[d]	200 nm	20 ms	N/A
HeLa cell, unlabelled	Fig S2	phase	4 V halogen lamp	Bright Line 582/75[c]	1	350 nm	20 ms	N/A
Polystyrene beads, 200nm	Fig. S3	phase	4 V halogen lamp	Bright Line 582/75[c]	50[d]	200 nm	20 ms	N/A
Human embryonic kidney HEK 293T cells, murine macrophage RAW 264.7 cells, mouse hippocampal primary neuron, human fibroblast, all unlabelled except for Alexa Fluor 647 immunolabelled α –synuclein aggregates in primary hippocampal neuron	Fig. S12	phase	4 V halogen lamp	Bright Line 582/75[c]	30-70[d]	200 nm	20 ms	N/A
HeLa cell, live	Fig. S13	phase	4 V halogen lamp	Bright Line 582/75[c]	> 60	350 nm	0.03 Hz	> 33 min
HeLa cell expressing Vimentin-Dreiklang	Fig. S14	SOFI	800 W cm^{-2} at 532 nm 8.5 W cm^{-2} at 405 nm	Bright Line 582/75[c]	1500	350 nm	50 Hz	30 s
		phase	4 V halogen lamp		5000	350 nm	50 Hz	100 s

[a]measured near the back focal plane of the objective for fluorescence illumination, [b]Chroma, [c]Semrock, [d]z-stack stage scanning, all other experiments were performed with multi-plane acquisition, [e]for single frame imaging, the exposure time is indicated

Table S2. Imaging and Analysis Parameters.

24

Combined Multi-Plane Phase Retrieval and Super-Resolution Optical Fluctuation Imaging for 4D Cell Microscopy - Supplementary Material
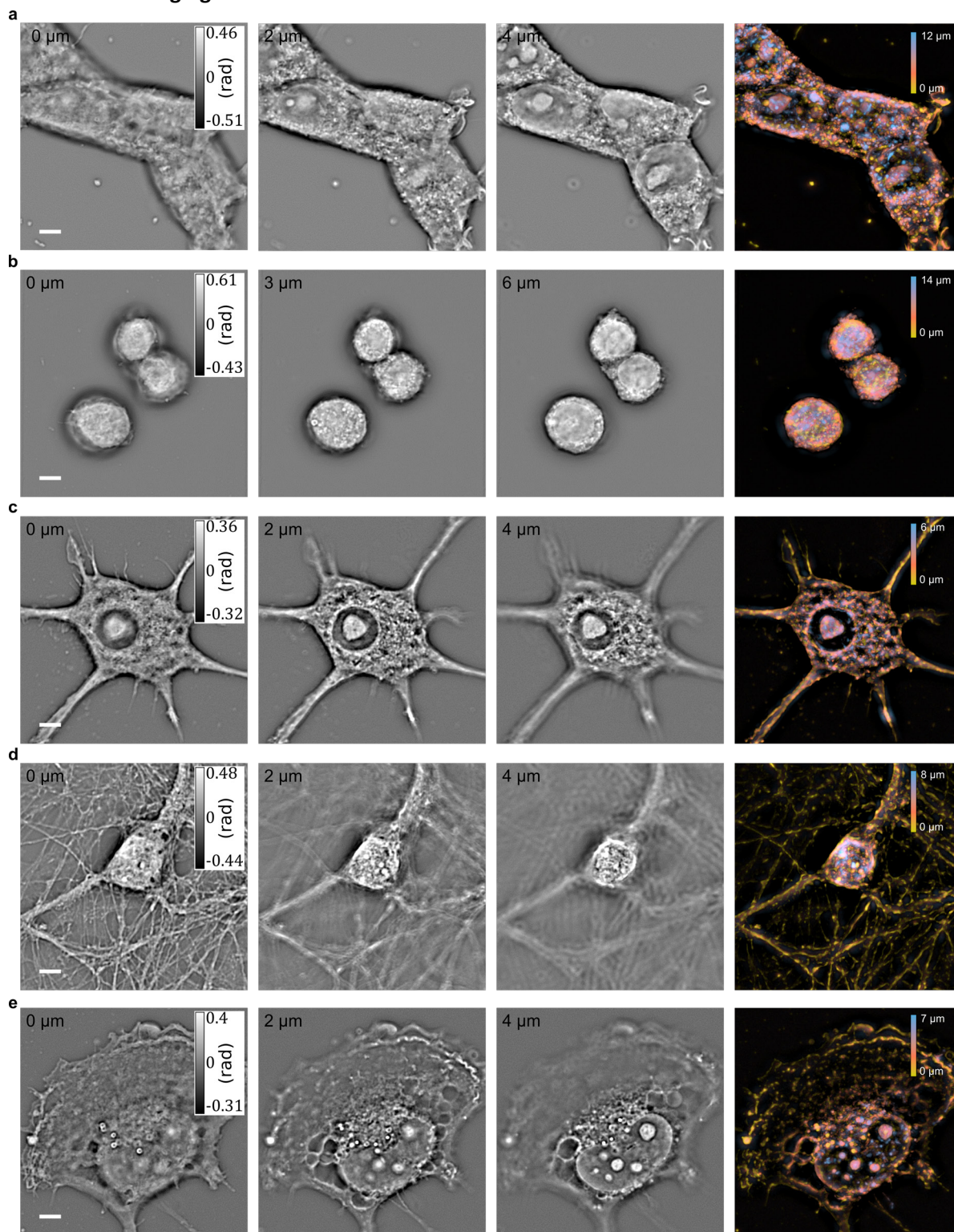
8.2   Phase imaging

Figure S18: Phase imaging of fixed cell samples using large image stacks. Samples were scanned with $\Delta z = 200$ nm and x-y-slices at different height along with a color-coded maximum intensity-z-projection of images with a phase threshold = 0 are shown for each cell type. Phase in radian. (a) Human embryonic kidney HEK 293T cells, (b) murine macrophage RAW 264.7, (c) LPS stimulated murine macrophage RAW 264.7, (d) mouse hippocampal primary neuron, (e) human fibroblast. Scale bar 5 µm
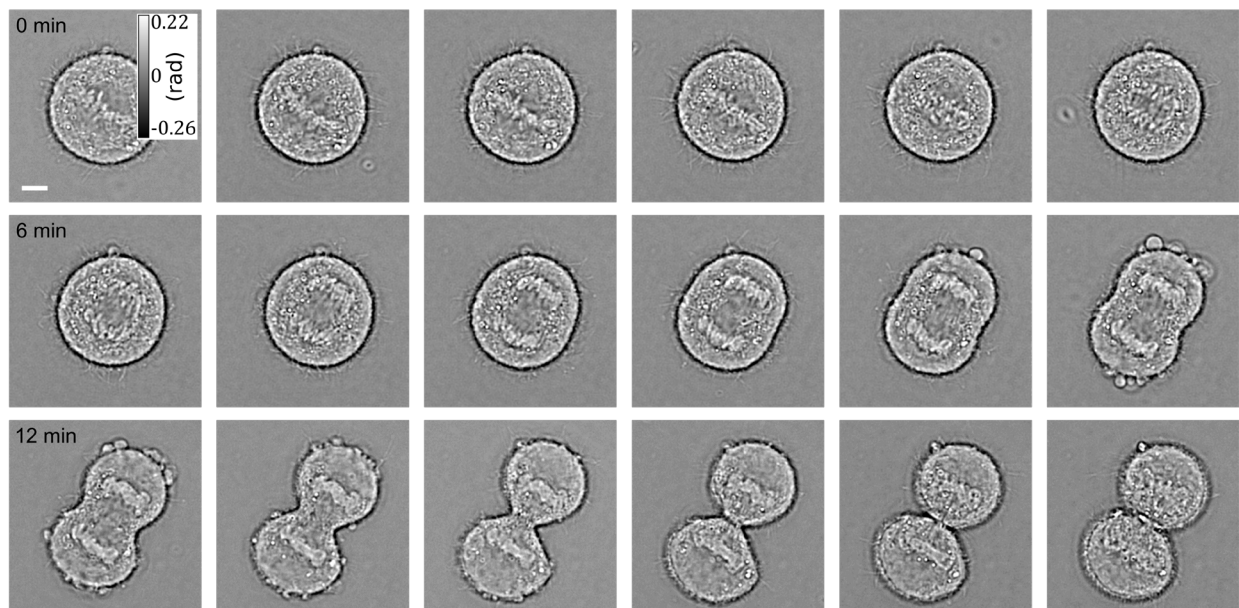
Figure S19: Dividing HeLa cell. Living HeLa cell imaged every 30 s as it undergoes mitosis from metaphase to telophase using the MP phase microscope (every second image is shown for plane 7). The phase is given in radian. Scale bar 5 µm.
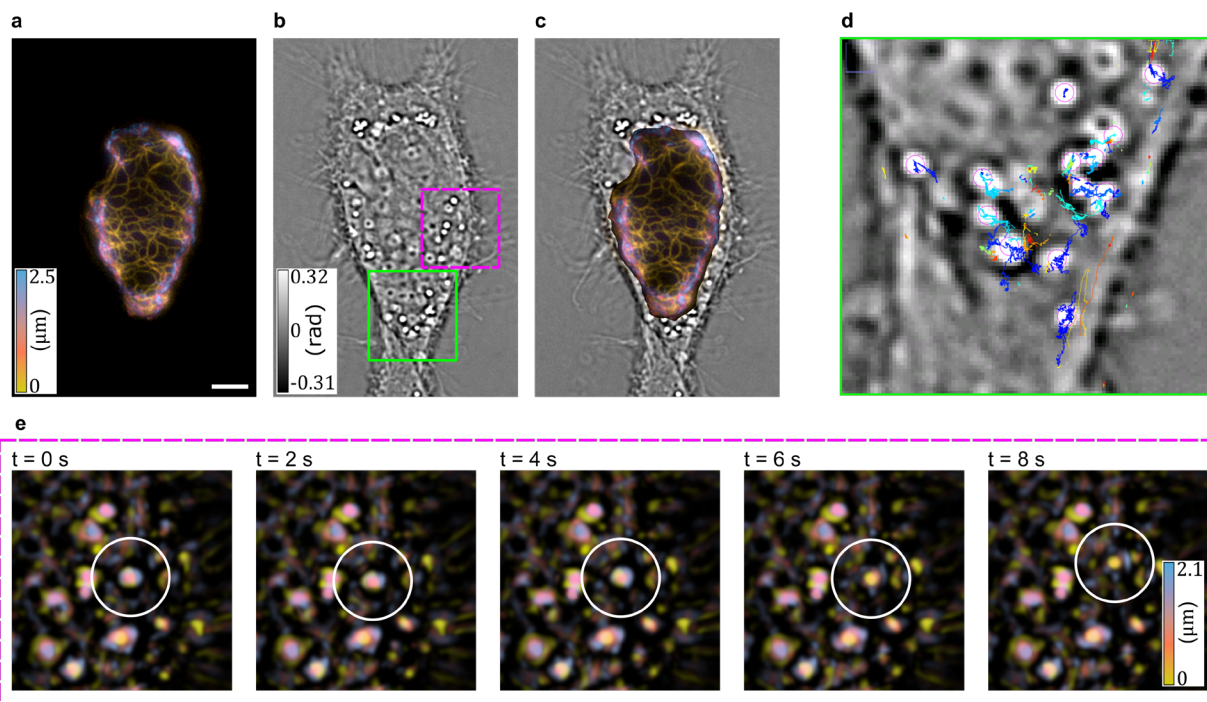

Figure S20 Multi-plane SOFI and dynamic phase imaging. (a) SOFI maximum intensity projection of a living HeLa cell expressing Vimentin-Dreiklang. (b) First frame of a 100 s 3D phase movie imaged at 50 Hz. (c) Overlay of 3D SOFI and phase. (d) Example tracking of highly scattering vesicles in a region of interest (green) using TrackMate. (e) Phase maximum intensity projection (Threshold T = 0 rad) for selected time point displaying 3D dynamics. Scale bar 5 µm.

Combined Multi-Plane Phase Retrieval and Super-Resolution Optical Fluctuation Imaging for 4D Cell Microscopy - Supplementary Material

8.3 Fluorescent beads calibration sample preparation

Fluorescent beads (PS-Speck™ Microscope Point Source Kit, orange and deep red, Thermo Fisher Scientific) with a diameter of 0.175 µm were allowed to dry in a Lab-tek® II chambered cover slide (nunc) and subsequently covered with the provided immersion medium.

8.4 Polystyrene beads sample preparation

Polybead® Polystyrene 0.2 Micron Microspheres (2.57 % Solids-Latex) (Polysciences Inc.) were diluted 1:100 in Millipore water followed by 1:100 dilution in 0.5 % agarose solution. 100-200 µl of this mixture were dispersed on a coverslip (0.17 mm thickness (Assistent)) for imaging. An intensity stack of 50 µm x 50 µm x 10 µm (50 planes spaced by 200 nm) has been acquired and processed to recover the corresponding phase.

8.5 Atomic Force Microscopy (AFM) sample preparation and measurement

Cleanroom fabrication was performed in the Center of MicroNanoTechnology (CMi, EPFL) following standard protocols:

1. Pyrex/ glass wafers with a thickness of 145 ± 15 µm were coated with aluminium on the backside with a thickness of 500nm.
2. Photolithography: The AZ1512 photoresist was spin-coated on the top of the wafer to a final thickness of 1 µm. The wafer was then baked at 112 °C for 1 min 30 s. The exposure was performed using the MJB4 tool (Süss) for 0.8 s using a custom made mask, followed by development using the developer AZ for 55-65 s.
3. Dry etching: Reactive ion etching was performed using a C_4F_8 and O_2 based plasma on the LPX machine (SPTS Technologies). The etch time was 30 s and the photoresist was removed by O_2 plasma in the same machine by a consecutive processing step for 1 min.

Process 2. and 3. were repeated overall 3 times until the desired pattern was made.

4. The backside aluminium layer was removed by wet etching in ANP solution for 4 min.

AFM imaging was performed with the Dimension Icon (Bruker) in tapping mode in air. The used AFM tip was a RTESPA-525 and the height sensor data image was acquired with 0.5Hz with a resolution of 1024 pixels x1024 pixels on a scan area of 70 µm x 70 µm.

9 Bibliography

1. Born, M. & Wolf, E. *Principles of Optics, 7th (expanded) ed*. *Cambridge U. Press, Cambridge, UK* (1999).

2. Singer, W. & Brenner, K.-H. Transition of the scalar field at a refracting surface in the generalized Kirchhoff diffraction theory. *J. Opt. Soc. Am. A* **12,** 1913 (1995).

3. Singer, W., Totzeck, M. & Gross, H. *Handbook of optical systems, physical image formation*. **2,** (John Wiley & Sons, 2006).

4. Singer, W. & Brenner, K.-H. Transition of the scalar field at a refracting surface in the generalized Kirchhoff diffraction theory. *J. Opt. Soc. Am. A* **12,** 1913 (1995).

27

Combined Multi-Plane Phase Retrieval and Super-Resolution Optical Fluctuation Imaging for 4D Cell Microscopy - Supplementary Material

5. Mandel, L. & Wolf, E. *Optical coherence and quantum optics*. (Cambridge University Press, 1995).

6. Streibl, N. Three-dimensional imaging by a microscope. *J. Opt. Soc. Am. A* **2,** 121 (1985).

7. McCutchen, C. W. Generalized aperture and the three-dimensional diffraction image. *J. Opt. Soc. Am. A* **54,** 240–244 (1964).

8. Titchmarsh, E. C. *Introduction to the theory of Fourier integrals*. **2,** (Clarendon Press Oxford, 1948).

9. Nguyen, T. H., Edwards, C., Goddard, L. L. & Popescu, G. Quantitative phase imaging with partially coherent illumination. *Opt. Lett.* **39,** 5511–5514 (2014).

10. Streibl, N. Phase imaging by the transport equation of intensity. *Opt. Commun.* **49,** 6–10 (1984).

11. Kim, T., Edwards, C., Goddard, L. L. & Popescu, G. Quantitative phase imaging with programmable illumination. in *Proc. SPIE* **9336,** 93361F (2015).

12. Abràmoff, M. D., Magalhães, P. J. & Ram, S. J. Image processing with ImageJ. *Biophotonics Int.* **11,** 36–42 (2004).

13. Shannon, C. E. Communication in the presence of noise. *Proc. IRE* **37,** 10–21 (1949).

14. Geissbuehler, S. *et al.* Live-cell multiplane three-dimensional super-resolution optical fluctuation imaging. *Nat Commun* **5,** 1–7 (2014).

15. Deschout, H. *et al.* Complementarity of PALM and SOFI for super-resolution live-cell imaging of focal adhesions. *Nat. Commun.* **7,** 13693 (2016).

16. Peeters, Y. *et al.* Correcting for photodestruction in super-resolution optical fluctuation imaging. *Sci. Rep.* **7,** (2017).

17. Dertinger, T., Colyer, R., Vogel, R., Enderlein, J. & Weiss, S. Achieving increased resolution and more pixels with Superresolution Optical Fluctuation Imaging (SOFI). *Opt. Express* **18,** 18875–18885 (2010).

18. Geissbuehler, S. *et al.* Mapping molecular statistics with balanced super-resolution optical fluctuation imaging (bSOFI). *Opt. Nanoscopy* **1,** 1–7 (2012).